The Astrophysical Journal, 799:223 (7pp), 2015 February 1 doi:10.1088/0004-637X/799/2/223

THE EFFECT OF A DYNAMIC INNER HELIOSHEATH THICKNESS ON COSMIC-RAY MODULATION

R. Manuel, S. E. S. Ferreira, and M. S. Potgieter
Centre for Space Research, North-West University, Potchefstroom 2520, South Africa; rexmanuel@live.com
Received 2014 September 18; accepted 2014 December 7; published 2015 January 30

ABSTRACT

The time-dependent modulation of galactic cosmic rays in the heliosphere is studied over different polarity cycles by computing 2.5 GV proton intensities using a two-dimensional, time-dependent modulation model. By incorporating recent theoretical advances in the relevant transport parameters in the model, we showed in previous work that this approach gave realistic computed intensities over a solar cycle. New in this work is that a time dependence of the solar wind termination shock (TS) position is implemented in our model to study the effect of a dynamic inner heliosheath thickness (the region between the TS and heliopause) on the solar modulation of galactic cosmic rays. The study reveals that changes in the inner heliosheath thickness, arising from a time-dependent shock position, does affect cosmic-ray intensities everywhere in the heliosphere over a solar cycle, with the smallest effect in the innermost heliosphere. A time-dependent TS position causes a phase difference between the solar activity periods and the corresponding intensity periods. The maximum intensities in response to a solar minimum activity period are found to be dependent on the time-dependent TS profile. It is found that changing the width of the inner heliosheath with time over a solar cycle can shift the time of when the maximum or minimum cosmic-ray intensities occur at various distances throughout the heliosphere, but more significantly in the outer heliosphere. The time-dependent extent of the inner heliosheath, as affected by solar activity conditions, is thus an additional time-dependent factor to be considered in the long-term modulation of cosmic rays.

Key words: cosmic rays – diffusion – Sun: activity – Sun: heliosphere

1. INTRODUCTION

Cosmic rays are subject to an ∼11 yr modulation cycle, which is anti-correlated to the ∼11 yr solar activity cycle. During solar maximum periods, lower cosmic-ray intensities are recorded while higher intensities are recorded during solar minimum periods. These particles, once they enter the heliosphere, are modulated by four major modulation process: convection, energy losses/gains, diffusion, and drifts. In order to model long-term cosmic-ray modulation in the heliosphere, le Roux & Potgieter (1995) combined drift effects and global merged interaction regions into their two-dimensional (2D) time-dependent drift model to successfully simulate an 11 and a 22 yr cosmic-ray modulation cycle. Later, Ferreira & Potgieter (2004) developed the compound approach considering time-dependent global changes in the heliospheric magnetic field (HMF) and the heliospheric current sheet (HCS) tilt angle, α, to construct a time dependence for all transport coefficients. Recently, Manuel et al. (2011b, 2014) improved this compound approach by introducing theoretical advances in the drift and diffusion coefficients into the time-dependent transport model to compute cosmic-ray modulation in the heliosphere over several cycles. New in this work is that a time-dependent termination shock (TS) position is introduced and its effect on cosmic-ray modulation in the heliosphere is shown over different solar cycles.

The heliosphere, which is the entire region of space influenced by the Sun and its magnetic field, is formed as the solar wind, which blows radially outward from the Sun, encounters the local interstellar medium (LISM). The boundary layer that separates the solar wind plasma from the interstellar plasma is called the heliopause (HP). Due to this encounter, the solar wind suddenly decreases to a subsonic speed forming a shock region called the TS. Since the heliosphere is a dynamic structure, the TS position, r_{ts}, responds to variations of the solar wind speed and solar wind density, which change over a ∼11 yr solar cycle (Scherer & Fahr 2003). An increase in either the density or the velocity of the solar wind (or LISM) would result in a TS forming at larger (or smaller in the case of LISM density or velocity increase) heliocentric distances (see, e.g., Wang & Belcher 1999; Scherer & Fahr 2003; Whang et al. 2004; Scherer & Ferreira 2005a, 2005b; Washimi et al. 2011).

Whang et al. (1995) proposed that the location of the TS is anti-correlated with solar activity, i.e., the TS is located farther away from the Sun during solar minimum periods and closer to the Sun during solar maximum periods. Later, Wang & Belcher (1999) proposed that the location of the TS oscillates approximately 13 AU per solar cycle in response to the ∼11 yr solar cycle, and it moves outward faster than it moves inward. It was shown by Scherer & Ferreira (2005a, 2005b) that such changes in the geometry of the heliosphere also influence the cosmic-ray particle distribution inside the heliosphere.

Observations by both *Voyager* spacecraft confirmed the existence of a dynamic TS. During the TS crossing of *Voyager 1*, the TS was moving inward toward the Sun (Stone et al. 2005). However, during the TS crossing of *Voyager 2*, it was moving outward with respect to the Sun and had remained near the spacecraft for nearly a year, and then moved inward rapidly toward the Sun (Richardson & Wang 2011). A TS position of 10 AU closer to the Sun along the *Voyager 2* trajectory, compared to that of *Voyager 1*, suggests a possible asymmetric structure of the TS and/or a time dependence in the TS position.

Work done by Snyman (2007), Webber & Intriligator (2011), Richardson & Wang (2011, 2012), and Washimi et al. (2011) showed the computed time-dependent profile of the TS radius from the Sun using various models. Snyman (2007) for example, used a 2D hydrodynamic model and showed that any short-term variations in solar wind density and velocity will induce waves of increased and decreased dynamic pressure in the solar wind and the position of the TS will move inward or outward with respect to the Sun in response to these changes. Webber & Intriligator (2011) also computed the TS distance as a function of time along both *Voyager* trajectories using the solar wind plasma data

from *Voyager 2*, *ACE*, and *OMNI*. The plasma data from these spacecraft were used to compute the solar wind ram pressure, which was then used to calculate the location of the TS (see also Webber 2005). Washimi et al. (2011) computed the TS position using a three-dimensional magnetohydrodynamic model that includes the effect of neutral particles and Richardson & Wang (2011) computed the TS position using a 2D hydrodynamic model that includes the effect of pickup ions. The former authors used *Voyager 2* observations while the latter used *OMNI* observations along with *Voyager 2* observations to calculate the time-dependent TS position.

The TS radius as found by the abovementioned authors varies from ∼75 AU to ∼95 AU, translating into a ∼20 AU change in position over a solar cycle. First, the effect of extreme r_{ts} values, namely 75 AU and 95 AU, on proton intensities are shown. Later, two time-dependent profiles of the TS position, which varies from 80 AU to 90 AU over a solar cycle, are introduced to study its effect on time-dependent cosmic-ray modulation in the heliosphere. The modulation boundary (r_{hp}) is assumed at 120 AU so that the width of the inner heliosheath varies between 30 AU and 40 AU. The measured cosmic-ray intensities of *Voyager 1* at this distance are used as the boundary spectrum (also called the HP spectrum; see Potgieter et al. 2014) in this study.

2. MODULATION MODEL

The numerical model used in this work is based on a 2D time-dependent transport model in which the Parker (1965) transport equation is solved in terms of time, t, and rigidity, P, in (r, θ) space where r is the radial distance in AU and θ is the polar angle. The rigidity is defined as $P = pc/q$ with p being the particle's momentum, q its charge, and c the speed of light, with rigidity steps $\Delta \ln P = 0.08$. We assumed the grid size in r as $\Delta r = 0.6$ AU and in θ as $\Delta\theta = 2.^{\circ}5$. The time steps are chosen such that solar cycle related changes propagate with the solar wind speed.

The drift coefficient as given by Burger et al. (2000) is used in this work. However, a time-dependent function, $f_1(t)$, is used to scale the drift coefficient to minimum values for extreme solar maximum periods and to maximum values for solar minimum periods. The drift coefficient is given by

$$K_A = K_{A0}\frac{\beta P}{3B}\frac{10P^2}{10P^2+1} f_1(t) \quad \text{for } r < r_{ts}, \tag{1}$$

and

$$K_A = K_{A0}\frac{\beta P}{3B}\frac{10P^2}{10P^2+1}\left(\frac{r_{ts}}{r}\right)^6 f_1(t) \quad \text{for } r \geqslant r_{ts}, \tag{2}$$

where K_{A0} is a dimensionless constant, r_{ts} is the TS position in AU, B is the HMF magnitude, and β is the ratio between the particle speed to the speed of light. For details, see Manuel et al. (2011b, 2014).

The important diffusion coefficients in a heliocentric spherical coordinate system are, respectively,

$$K_{rr} = K_{||}\cos^2\psi + K_{\perp r}\sin^2\psi, \quad \text{and} \tag{3}$$

$$K_{\theta\theta} = K_{\perp\theta}. \tag{4}$$

Here K_{rr} is the effective diffusion coefficient in the radial direction and $K_{\theta\theta}$ is the effective diffusion coefficient in the polar direction, with $K_{||}$ being the diffusion coefficient parallel to the HMF, $K_{\perp r}$ the perpendicular diffusion coefficient in the radial direction, $K_{\perp\theta}$ the perpendicular diffusion coefficient in the polar direction, and ψ the spiral angle of the HMF.

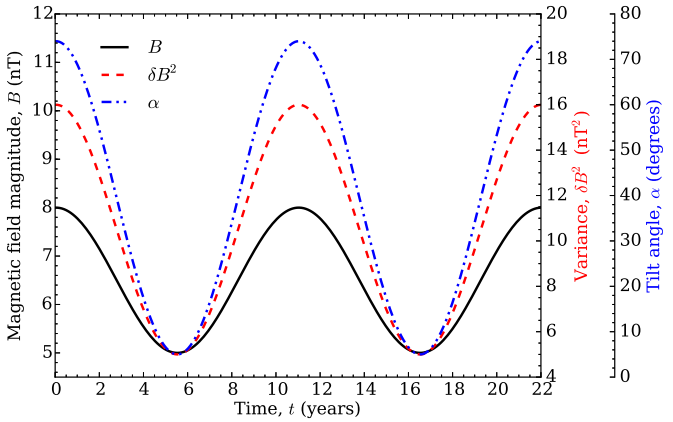

Figure 1. Assumed HMF magnitude (B), variance (δB^2), and tilt angle (α) used in the model over a 22 yr period.

Because only energies of a few GeV and above are considered, we assume a rigidity dependence for $K_{||}$ as calculated by Teufel & Schlickeiser (2002) for protons in the inner heliosphere,

$$K_{||} = \frac{C_1 v}{3}\left(\frac{P}{P_0}\right)^{\frac{1}{3}}\left(\frac{r}{r_0}\right)^{C_2} f_2(t) \quad \text{for } r < r_{ts} \tag{5}$$

and

$$K_{||} = \frac{C_1 v}{3 s_k}\left(\frac{P}{P_0}\right)^{\frac{1}{3}}\left(\frac{r}{r_0}\right)^{C_2}\left(\frac{r_{ts}}{r}\right) f_2(t) \quad \text{for } r \geqslant r_{ts}, \tag{6}$$

where C_1 is a constant, $P_0 = 1$ MV, $r_0 = 1$ AU, C_2 a constant, s_k is the TS compression ratio, v is the particle speed, and $f_2(t)$ a time-dependent function.

For the two perpendicular diffusion coefficients, we assume

$$K_{\perp r} = a K_{||}\frac{f_3(t)}{f_2(t)} \tag{7}$$

$$K_{\perp\theta} = b K_{||} F(\theta)\frac{f_3(t)}{f_2(t)}, \tag{8}$$

where $a = 0.02$, $b = 0.01$, $F(\theta)$ is a function enhancing $K_{\perp\theta}$ toward the poles by a factor of nine (Potgieter 2000; Ferreira & Potgieter 2004), and $f_3(t)$ is a time-varying function. These equations are divided by $f_2(t)$ to remove the time dependence of $K_{||}$ (from Equation (5)) and multiplied by $f_3(t)$ to describe only the time dependence of $K_{\perp}$ (see Manuel et al. 2014, for details).

To construct the time-dependent functions $f_1(t)$, $f_2(t)$, and $f_3(t)$, the theoretical advances by Shalchi et al. (2004), Teufel & Schlickeiser (2002, 2003), and Minnie et al. (2007) are used and incorporated into our time-dependent transport model. These authors showed how the diffusion and drift coefficients depend on basic turbulence quantities such as the HMF magnitude (B) and variance (δB^2), which change over a solar cycle. See Manuel et al. (2011a, 2011b, 2014) for full details. As discussed in our previous work, the time-dependent transport coefficients require B, δB^2, and tilt angle (α) as input parameters that are then transported from Earth radially out with solar wind speed into the outer heliosphere. Figure 1 shows B, δB^2, and α used in this work, which are assumed to vary over two 11 yr solar cycles. These input parameters are assumed to vary

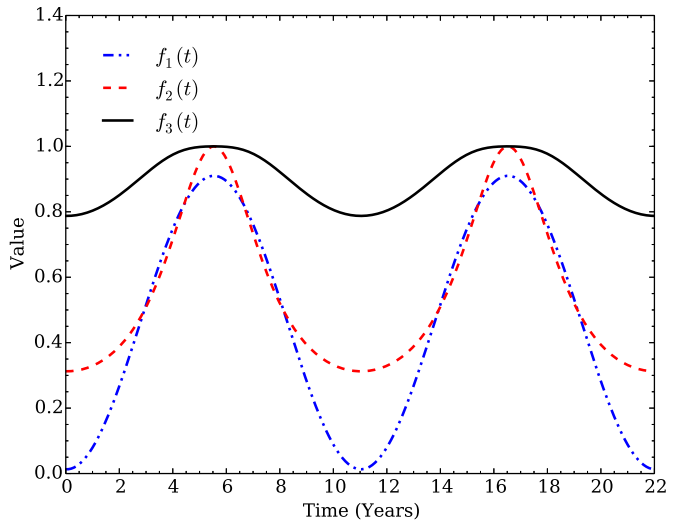

Figure 2. Values of the time-dependent functions $f_1(t)$ in Equation (9), $f_2(t)$ in Equation (10), and $f_3(t)$ in Equation (11) plotted as a function of time.

such that B changes from 5 nT to 8 nT, δB^2 from 5 nT^2 to 16 nT^2, and α from 5° to 75° in response to changing solar activity, from solar minimum to maximum periods. Note that smooth sinusoidal functions, symmetric with respect to solar minimum, are used instead of observed values to clearly illustrate the effect of an oscillating TS position on computed intensities.

A time dependence for the drift coefficient K_A is constructed similar to the theoretical work of Minnie et al. (2007), where K_A is changing over a solar cycle and is given by

$$f_1(t) = \frac{0.013(75.0 - \alpha(t))}{\alpha_c}, \quad (9)$$

with $\alpha_c = 1°$. See also Manuel et al. (2014).

The time dependence for $K_{||}$ is attained from an expression for the parallel free-mean path $\lambda_{||}$ for protons given by Teufel & Schlickeiser (2003). Because our study is only applicable to higher rigidities, we approximate their complicated equation so that the time dependence of $K_{||}$ is given by

$$f_2(t) = C_4 \left(\frac{1}{\delta B(t)}\right)^2, \quad (10)$$

where C_4 is a constant in units of nT^2 (see also Manuel et al. 2014).

For the time dependence of the perpendicular diffusion coefficients, $f_3(t)$, we assume the expression for $\lambda_\perp$ (see Shalchi et al. 2004) is

$$f_3(t) = C_5 \left(\frac{\delta B(t)}{B(t)}\right)^{\frac{4}{3}} \left(\frac{1}{\delta B(t)}\right)^{\frac{2}{3}}, \quad (11)$$

where C_5 a constant in units of (nT)$^{2/3}$.

Figure 2 shows the time dependence of the drift coefficient, $f_1(t)$ (blue dash–dot-dot line), for which α is used as input parameter (as given in Equation (9)) and which varies from 0 to 0.9 from maximum to minimum solar activity. Also shown in the figure is the time dependence of the parallel and perpendicular diffusion coefficients, $f_2(t)$ and $f_3(t)$ in Equations (10) and (11), which use B and δB^2 as input parameters. Evidently, $f_2(t)$ varies between solar maximum and solar minimum by a factor of three while $f_3(t)$ only changes by a factor of 1.2 between solar maximum and minimum.

All the time-dependent effects are transported radially out with the solar wind speed. For solar minimum conditions, this radial speed varies from 400 km s^{-1} in the equatorial regions to 800 km s^{-1} at the poles while for solar maximum conditions, the speed is 400 km s^{-1} at all latitudes (see, e.g., Ferreira & Scherer 2006). At the TS, the radial solar wind speed decreases by a factor of $s_k = 3$ (Burlaga et al. 2005; Richardson et al. 2008) and then decreases as $1/r^2$ further out in the inner heliosheath to the HP (e.g., Strauss et al. 2010).

The *Voyager* observations of B in the inner heliosheath indicate that $B \propto r$ for $r > r_{ts}$ (Burlaga et al. 2007). The diffusion coefficients depend on B and are expected to change over the shock. For this study, Equation (5) is assumed for $r < r_{ts}$ and at the TS, the diffusion coefficient decreases with s_k (Burlaga et al. 2005; Richardson et al. 2008), then scales as $1/r$ up to the HP, as given by Equation (6). To calculate the cosmic-ray intensities in the heliosphere, Florinski et al. (2003), Ferreira & Scherer (2006), Ferreira et al. (2007a, 2007b), Luo et al. (2013), Potgieter et al. (2014), and Zhao et al. (2014) made similar assumptions about the diffusion coefficients, assuming that they are to the first-order inversely proportional to B.

3. MODELING

In this section, the term heliosheath will be used to refer to the inner heliosheath. Before implementing a dynamic TS position in the model, the computed intensity contour profiles in the heliosphere are shown as reference solutions for extreme r_{ts} values with different snapshots of solar activity. Note that all the diffusion and drift coefficients are scaled time-dependently over a solar cycle as discussed above.

The computed cosmic-ray distribution in the heliosphere from the heliospheric pole to the equatorial plane during different levels of solar activity and magnetic polarity cycles are shown in Figures 3–5 as contour plots. These figures illustrate how the cosmic-ray distribution in the heliosphere changes according to a changing r_{ts}. Figure 3 shows the 2.5 GV proton distribution for the $A < 0$ polarity cycle when $r_{ts} = 95$ AU (top panel) and $r_{ts} = 75$ AU (bottom panel). During an $A < 0$ polarity cycle, protons drift mainly into the inner heliosphere along the HCS and exit through the polar regions of the heliosphere. The figure shows that high cosmic-ray intensities are computed at the lower heliolatitudes compared to the polar regions during this period. The distribution for a $r_{ts} = 75$ AU snapshot, when compared to the $r_{ts} = 95$ AU snapshot ,gives lower intensities with a different distribution (different intensity gradients) inside the heliosphere due to a thicker heliosheath that acts as a modulation barrier. Although there is no acceleration of cosmic rays assumed in this model, the effect of the heliosheath is simulated by changing (decreasing) the transport parameters across the TS. This means that the heliosheath acts as a modulation barrier (Potgieter & le Roux 1989; Ferreira et al. 2004; Langner et al. 2004; Nkosi et al. 2011; Ngobeni & Potgieter 2012; Potgieter 2013) and increasing the thickness will result in fewer cosmic rays entering the heliosphere.

Figure 4 is similar to Figure 3 but for a solar maximum period. The figure shows that during solar maximum activity, there is no drift direction preference, as shown in Figure 3. The contour levels are spaced almost equally everywhere, meaning that the modulation process is diffusion dominated. Additionally, the effects of a thicker heliosheath during solar maximum activity is not nearly as evident as in Figure 3. Figure 5 is also similar

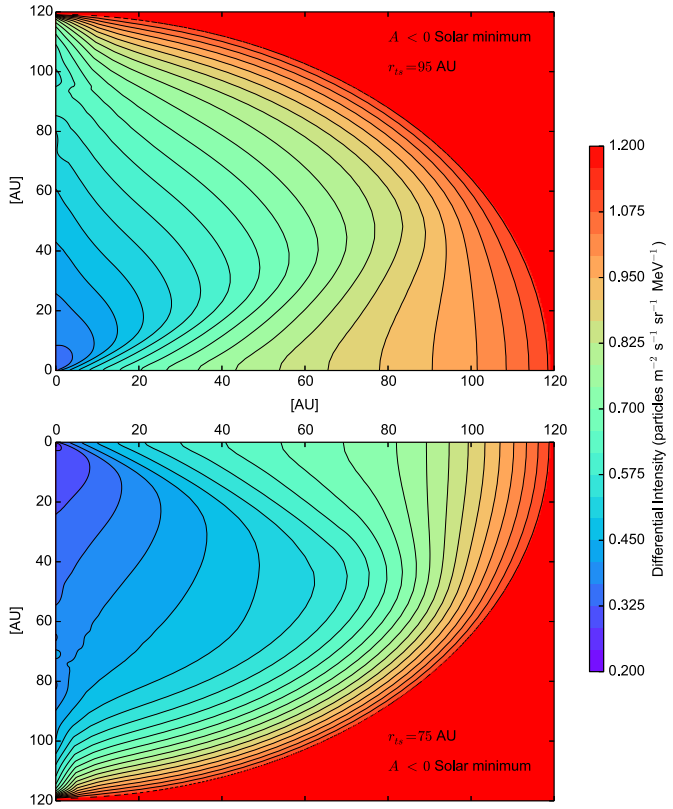

Figure 3. Contour plots show the intensity distribution of 2.5 GV protons in the heliosphere from the poles to the equatorial plane during an $A < 0$ solar minimum. The top panel shows the distribution when $r_{\rm ts} = 95$ AU and bottom panel shows the distribution when $r_{\rm ts} = 75$ AU.

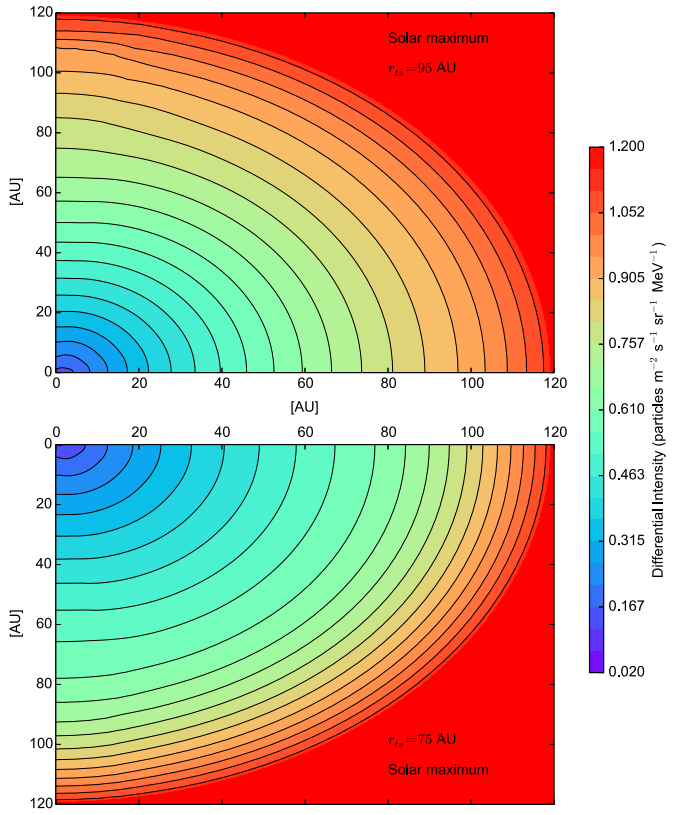

Figure 4. Similar to Figure 3, but for a solar maximum period.

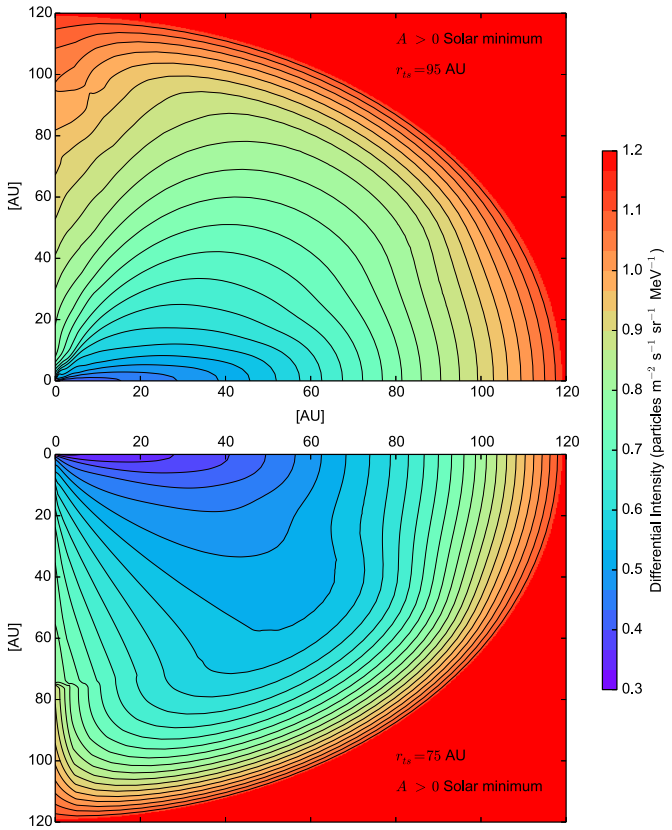

Figure 5. Similar to Figure 3, but for an $A > 0$ solar minimum.

to Figure 3 but for a solar minimum period with an $A > 0$ polarity. It now follows that protons enter the heliosphere mainly through the polar regions and exit along the HCS so that higher intensities are computed during this cycle in the polar regions compared to the equatorial plane for a given radial distance. The $r_{\rm ts} = 95$ AU (top panel) snapshot shows that more cosmic rays enter the heliosphere than with $r_{\rm ts} = 75$ AU (bottom panel), caused by a thinner heliosheath so that the distribution of protons is changed with heliolatitude. From these figures, it follows that a time-dependent heliosheath thickness changes the cosmic-ray distribution in the heliosphere significantly during solar minimum conditions. The thicker heliosheath is evidently causing a redistribution of cosmic rays. The radial dependence is obviously also changing in terms of latitude.

For this work, two polar angles, namely $\theta = 50^\circ$ and $\theta = 70^\circ$, are chosen to roughly represent the latitude of *Voyager 1* and *Voyager 2* (projected into one hemisphere) while traversing the outer heliosphere. This study is therefore useful in interpreting cosmic-ray measurements made by these spacecraft. The intensity ratios for the assumed $r_{\rm ts}$ scenarios 10 AU apart, $r_{\rm ts} = 80$ AU and $r_{\rm ts} = 90$ AU, in the 50° plane during $A < 0$ and $A > 0$ polarity cycles are shown in Figure 6 as a function of radial distance. The ratios for the $A < 0$ and $A > 0$ polarity cycles are shown as black solid and red dashed lines, respectively. The figure shows that for both the $A < 0$ and $A > 0$ polarity cycles the model gives almost the same ratio. In the heliosheath region, for both the $A < 0$ and $A > 0$ polarity cycles, the ratio increases from ~0.85 at ~80 AU to 1.0 at the boundary. The figure also shows the ratio of intensities corresponding to $r_{\rm ts} = 75$ AU and $r_{\rm ts} = 95$ AU for both the $A < 0$ and $A > 0$ polarity cycles as blue solid and green dashed lines, respectively. This is to show the effect of different $r_{\rm ts}$ values as also shown in the contour

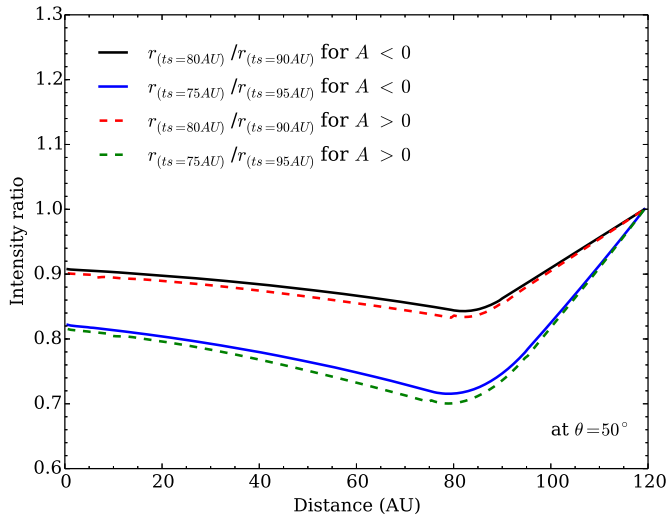

Figure 6. Ratio between computed 2.5 GV proton intensities for $r_{ts} = 80$ AU and $r_{ts} = 90$ AU, and for $r_{ts} = 75$ AU and $r_{ts} = 95$ AU, at $\theta = 50^\circ$, shown for both polarity cycles.

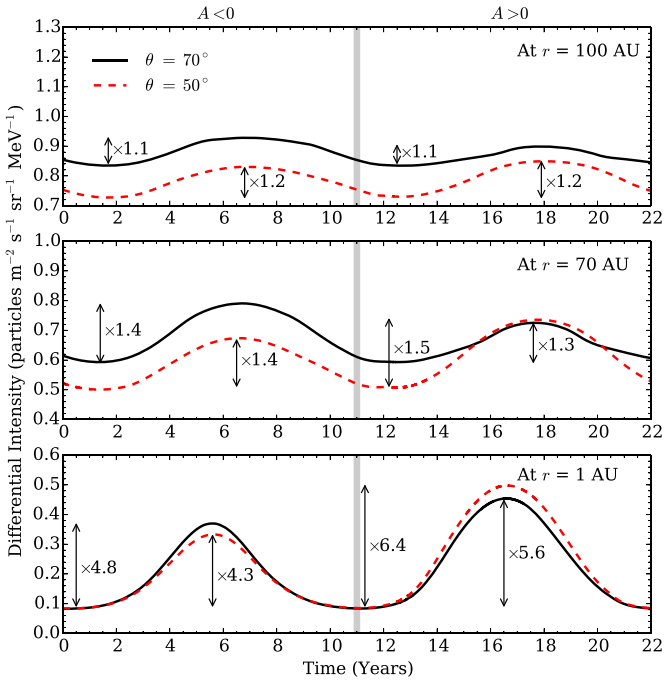

Figure 7. Computed 22 yr cycle for 2.5 GV protons with a stationary TS position, $r_{ts} = 90$ AU, at three different radial distances (r) and at two polar angles (θ). The intensities are shown at $r = 1$ AU (top), $r = 70$ AU (middle), and $r = 100$ AU (bottom) for $\theta = 70^\circ$ (solid line) and $\theta = 50^\circ$ (dashed line). The shaded area represents the period when there was a transition from the $A < 0$ to the $A > 0$ polarity cycle. The left panel shows the $A > 0$ cycle and the right panel shows the $A > 0$ cycle. The numbers indicate the factor of increase in intensity from the minimum level (solar maximum activity) to the corresponding maximum level (solar minimum activity). The largest effect/variation is evidently at Earth.

plots in Figures 3–5. From the figure, it follows that the ratio is found to decrease from 1.0 at 120 AU to ∼0.70 at ∼80 AU then increase to ∼0.82 at 1 AU. This shows that a 20 AU change in the r_{ts} value can lead to a ∼30% difference in computed intensities in the 50° plane while a 10 AU change can lead to ∼15% effect. We also found that the ratio between the intensities for $r_{ts} = 75$ AU and 95 AU (20 AU apart) in the 70° plane can lead to a ∼25% effect on modulation while a 10 AU apart r_{ts} leads to a ∼10% effect. From this it follows that in the outer heliosphere a 10 AU apart r_{ts} can lead to a ∼15% change in cosmic-ray intensities in the $\theta = 50^\circ$ plane (higher heliolatitude) when compared to the $\theta = 70^\circ$ plane (lower heliolatitude), where an ∼10% effect is computed.

Figure 7 shows the computed time-dependent proton (2.5 GV) intensity at three different radial distances and two different polar angles for an assumed stationary TS position, $r_{ts} = 90$ AU. Computed intensities over a 22 yr period are shown at 1 AU (bottom panel), 70 AU (middle panel), and 100 AU (top panel) for two polar angles, namely those at $\theta = 50^\circ$ and $\theta = 70^\circ$, respectively. The vertical shaded area represents the period when there was a transition from the $A < 0$ to the $A > 0$ polarity cycle. From the figure, it follows that because protons drift in mainly along the HCS during an $A < 0$ polarity cycle, higher intensities are computed at $\theta = 70^\circ$ (solid black lines) compared to $\theta = 50^\circ$ (dashed red lines) at all radial distances. However, during an $A > 0$ polarity cycle, the model gives higher intensities at $\theta = 50^\circ$ compared to the lower heliolatitudes, except in the heliosheath regions. The different factors by which intensities increases from minimum to maximum levels are shown in the figure.

At 1 AU in the $\theta = 70^\circ$ plane (bottom panel), the model gives a somewhat peak-like maximum intensity profile during the $A < 0$ period compared to the $A > 0$ polarity period, where a slightly flatter intensity profile is computed. The peak profile during an $A < 0$ polarity period is caused by protons drifting inward to the Sun along the HCS and thus is sensitive to any changes in this region. On the other hand, the flatter profile during an $A > 0$ polarity period is caused by protons drifting inward to the Sun through the polar regions, and thus is relatively insensitive to conditions in the equatorial region (Kota & Jokipii 1983). Note that the drift and diffusion coefficients are scaled over a solar cycle by the time-dependent functions $f_1(t)$, $f_2(t)$, and $f_3(t)$, as discussed above, resulting in a time profile where drift effects are not so evident as in, e.g., steady-state drift dominated models.

Evident from Figure 7 is that, as expected, the model gives maximum cosmic-ray intensities for solar minimum activity periods and minimum intensities during solar maximum periods. The 1 AU, 70 AU, and 100 AU scenarios show that the ratio between minimum and maximum intensity is decreasing with increasing radial distance, again as expected, for both polarity cycles and at both polar angles. For the $\theta = 70^\circ$ plane during an $A < 0$ polarity cycle, this ratio decreases from 4.8 at 1 AU to 1.4 at 70 AU and to 1.1 at 100 AU. For the $A > 0$ cycle, the corresponding ratios are decreasing from 5.6 at 1 AU to 1.3 at 70 AU and to 1.1 at 100 AU. Similarly for the $\theta = 50^\circ$ plane during an $A < 0$ polarity cycle, the ratio decreases from 4.3 at 1 AU to 1.4 at 70 AU and to 1.2 at 100 AU, and during an $A > 0$ polarity cycle from 6.4 at 1 AU to 1.5 at 70 AU and 1.2 at 100 AU.

This figure also shows that the computed maximum/minimum intensities are delayed in the outer heliosphere compared to the inner heliosphere since solar cycle related changes from the Sun needs to propagate out into the heliosphere. At 1 AU the first maximum intensity is computed at 5.5 yr, which is delayed by a year to 6.5 yr at 70 AU and at 100 AU to 6.8 yr.

Figure 8 shows the computed scenarios in the $\theta = 70^\circ$ plane at 1 AU (third panel from top), 70 AU (second panel from top), and 100 AU (top panel), along with the scenario corresponding to an assumed stationary TS position, $r_{ts} = 90$ AU (dotted line), and two scenarios corresponding to the TS oscillating between $r_{ts} = 80$ AU and $r_{ts} = 90$ AU given by r_{ts} profile 1 (solid line) and profile 2 (dashed line). Profile 1 and profile 2 are

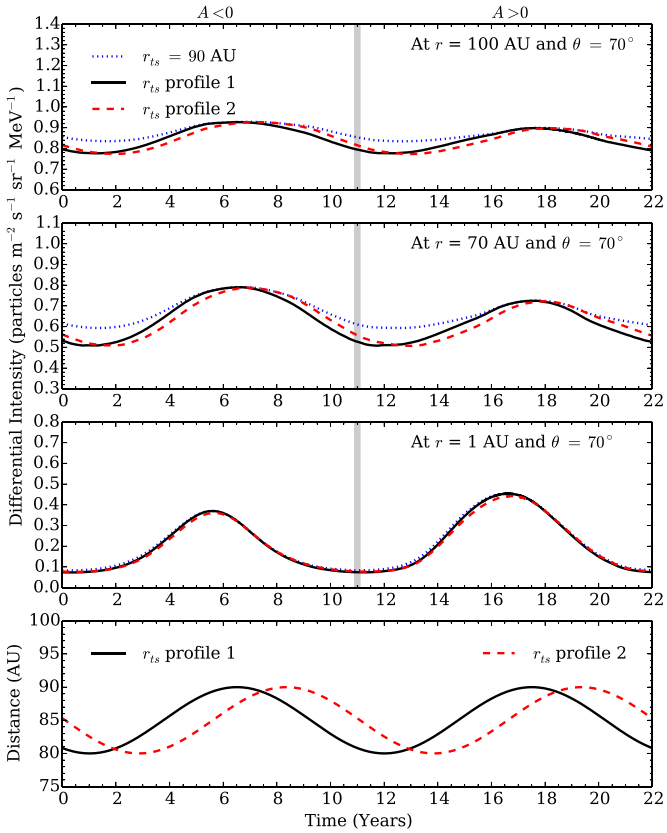

Figure 8. Computed 22 yr modulation cycle for 2.5 GV protons at three radial distances (r) for the assumed r_{ts} scenarios in the $\theta = 70^\circ$ plane. The intensities at $r = 1$ AU (third panel from top), $r = 70$ AU (second panel from top), and $r = 100$ AU (top panel) are shown with $r_{ts} = 90$ AU (blue dotted line), and two time-dependent r_{ts} scenarios, namely r_{ts} profile 1 (black solid line) and r_{ts} profile 2 (red dashed line), are shown in the bottom panel. The shaded area represents the period when there was a transition from the $A < 0$ to the $A > 0$ polarity cycle. The modulation boundary is at 120 AU.

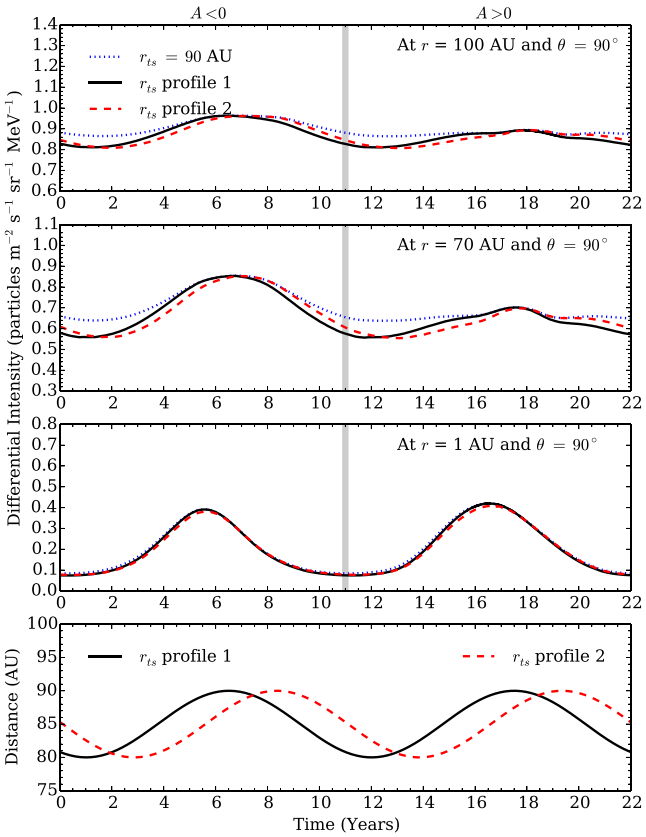

Figure 9. Similar to Figure 8, but for the 90° (equatorial) plane.

shown in the bottom panel. Note that both profiles have an 11 yr cycle and profiles are delayed by 1 yr and 2.75 yr (i.e., by a quarter of a cycle) when compared to the solar cycle. These profiles are introduced to illustrate the effect of r_{ts} delayed with respect to solar activity at 1 AU, as suggested by Richardson & Wang (2011), Snyman (2007), and Webber & Intriligator (2011). For all three scenarios in the figure, $r_{hp} = 120$ AU. It follows that the effect of a dynamic r_{ts} on computed intensities is related to the solar activity cycle, giving delays in the time when the maximum in intensity occurs at different radial distances, with the smallest effect at 1 AU. It also follows that at 1 AU, 70 AU, and 100 AU, the $r_{ts} = 90$ AU scenario gives the highest intensity at all radial distances when compared to profiles 1 and 2 because of the smaller heliosheath thickness. Although all time-dependent inputs are changing symmetrically around solar minimum/maximum, profiles 1 and 2 now produce intensities that are shifted in time with respect to what time dependence the solar activity related parameters follow. The intensity maximum computed during solar minimum period at 100 AU (top panel) is ahead by ~0.25 yr for profile 1 when compared to the $r_{ts} = 90$ AU scenario and is delayed by ~0.30 yr for profile 2. This lead and lag period computed for maximum intensity is found to be decreasing with distance from the HP to the Sun. At 70 AU (second panel from top), the maximum intensity for profile 1 is computed to be ~0.15 yr ahead compared to the $r_{ts} = 90$ AU scenario and ~0.25 yr delayed for profile 2. However, at 1 AU (third panel from top), the lag and lead period computed for maximum intensity is less significant and is found to be much less than ~0.1 yr for both profiles.

Table 1
Summary of the Time When Maximum Intensity Occurs during an $A < 0$ Polarity in the $\theta = 70^\circ$ Plane at Different Radial Distances for a Stationary TS Position at 90 AU and Two Oscillating TS Profiles, Namely 1 and 2, as Shown in Figure 8

	Time (yr)		
Radial Distance (r)	$r_{ts} = 90$ AU	r_{ts} Profile 1	r_{ts} Profile 2
1 AU	5.50	5.50	5.55
70 AU	6.50	6.35	6.75
100 AU	6.80	6.55	7.10

Figure 9 is similar to Figure 8 but for the $\theta = 90^\circ$ (equatorial) plane. The figure shows similar results when compared to the $\theta = 70^\circ$ plane. However, during an $A < 0$ polarity cycle, higher intensities are computed along $\theta = 90^\circ$ plane when compared to the $\theta = 70^\circ$ plane. These higher intensities are due to protons drifting along the HCS. During an $A > 0$ polarity cycle, lower intensities are computed along the $\theta = 90^\circ$ plane when compared to the $\theta = 70^\circ$ plane, again due to the drifts. It is found that during an $A < 0$ polarity cycle and for solar minimum conditions, the computed intensities along $\theta = 90^\circ$ plane at 1 AU, 70 AU, and 100 AU are increased by ~5%, ~8%, and ~4%, respectively, when compared to the $\theta = 70^\circ$ plane. During an $A > 0$ polarity cycle solar minima, the intensities are decreased by ~10%, ~3%, and ~1%, respectively, at these distances.

A summary of the time when maximum intensities occur, computed during an $A < 0$ polarity cycle, in the $\theta = 70^\circ$ plane at different radial distances for the three scenarios, is shown in Table 1. Similar results are also computed in the $\theta = 50^\circ$

and 90° planes but not shown here. Note how the delay in the occurrence of maximum cosmic rays between 1AU and 100 AU changes from the first to the other scenarios. From this we can conclude that the cosmic-ray intensities are affected throughout the heliosphere by a time-dependent TS position, i.e., a varying inner heliosheath width, with the largest effects in the outer heliosphere. It is thus found that changing the width of the inner heliosheath with time over a solar cycle can shift the time of when the maximum cosmic-ray intensities occur at various distance throughout the heliosphere, evidently more significantly in the outer heliosphere.

The effect of a dynamic inner heliosheath thickness on lower energies was also studied. Results are not shown, but it was found that a time-dependent TS position also has an effect on low-energy proton intensities. This will be discussed in our next paper.

4. CONCLUSIONS

A time-dependent, 2D model for the modulation of galactic cosmic rays in the heliosphere was used to simulate a period of 22 yr. The model incorporated recent theoretical advances in transport parameters (see also Manuel et al. 2011b, 2014), and for the first time, a time dependence in the solar wind TS position is incorporated into the model to study the effect of the dynamic inner heliosheath thickness on the solar modulation of galactic cosmic rays. From the study, it follows that any changes in the inner heliosheath thickness over a solar cycle affect cosmic-ray intensities everywhere in the heliosphere, with the smallest effect in the innermost heliosphere. We find that an increase in the inner heliosheath thickness causes fewer cosmic rays to arrive inside the heliosphere so that the spatial distribution of intensity is significantly effected. The large radial gradients that are evident from the computed intensity profiles in the outer heliosphere during both $A > 0$ and $A < 0$ polarity cycles show that the inner heliosheath region indeed acts as a modulation barrier. It is also found that a thicker heliosheath causes a redistribution of cosmic rays in terms of latitude.

We found that when the inner heliosheath thickness is changed, the computed proton intensities at higher heliolatitudes are more effected than the lower heliolatitudes. The computed intensities in $\theta = 50°$ plane shows that a time dependence of the inner heliosheath thickness with a 10 AU oscillating TS position affects the intensities by as much as ∼15% while a 20 AU oscillating TS position affects the intensity to ∼30%. The intensities in the $\theta = 70°$ plane show that there is a ∼10% effect on modulation for a 10 AU oscillating TS position and ∼25% effect for a 20 AU oscillating TS position.

Although sinusoidal functions are used for input parameters, asymmetric cosmic-ray intensity profiles are computed around solar minimum/maximum periods when an oscillating TS position is introduced. This asymmetry in the intensities around solar minimum/maximum activity is caused by the time dependence of r_{ts}, which is not in phase with the rest of the time-dependent parameters. The study shows that a time-dependent inner heliosheath thickness is found to have a significant effect on the cosmic-ray distribution in the heliosphere. An oscillating TS position causes a phase difference between the solar activity periods and the corresponding computed intensity periods. Also, it is found that the maximum intensities in response to a solar minimum activity period, especially in the outer heliosphere, could be observed early or later depending on the time-dependent TS profile. It is concluded that changing the width of the inner heliosheath with time over a solar cycle can shift the time when the maximum (or minimum) cosmic-ray intensities occur at various distance throughout the heliosphere, but more significantly in the outer heliosphere. The time-dependent extent of the inner heliosheath, as affected by solar activity conditions, is thus an additional time-dependent factor to be considered in the long-term modulation of cosmic rays.

This work is based on the research supported in part by the South African National Research Foundation (NRF). Any opinion, finding, conclusion, or recommendation expressed in this material is that of the author(s) and the NRF does not accept any liability in this regard. M.S.P. acknowledges the financial support of the NRF under the Incentive and Competitive Funding for Rated Researchers, grant Nos. 87820 and 68198. M.S.P. also appreciates discussions during the two team meetings on "Heliosheath Processes and Structure of the Heliopause: Modeling Energetic Particles, Cosmic Rays, and Magnetic Fields" hosted and supported by the International Space Science Institute in Bern, Switzerland.

REFERENCES

Burger, R. A., Potgieter, M. S., & Heber, B. 2000, JGR, 105, 27447
Burlaga, L. F., Ness, N. F., & Acuña, M. H. 2007, ApJ, 668, 1246
Burlaga, L. F., Ness, N. F., Acuña, M. H., et al. 2005, Sci, 309, 2027
Ferreira, S. E. S., & Potgieter, M. S. 2004, ApJ, 603, 744
Ferreira, S. E. S., Potgieter, M. S., & Scherer, K. 2007a, ApJ, 659, 1777
Ferreira, S. E. S., Potgieter, M. S., & Scherer, K. 2007b, JGR, 112, 1
Ferreira, S. E. S., Potgieter, M. S., & Webber, W. R. 2004, AdSpR, 34, 126
Ferreira, S. E. S., & Scherer, K. 2006, ApJ, 642, 1256
Florinski, V., Zank, G. P., & Pogorelov, N. V. 2003, JGR, 108, 1228 SSH 1: 1
Kota, J., & Jokipii, J. R. 1983, ApJ, 265, 573
Langner, U. W., Potgieter, M. S., & Webber, W. R. 2004, AdSpR, 34, 138
le Roux, J. A., & Potgieter, M. S. 1995, ApJ, 442, 847
Luo, X., Zhang, M., Rassoul, H. K., Pogorelov, N. V., & Heerikhuisen, J. 2013, ApJ, 764, 1
Manuel, R., Ferreira, S. E. S., & Potgieter, M. S. 2011a, AdSpR, 48, 874
Manuel, R., Ferreira, S. E. S., & Potgieter, M. S. 2014, SoPh, 289, 2207
Manuel, R., Ferreira, S. E. S., Potgieter, M. S., Strauss, R. D., & Engelbrecht, N. E. 2011b, AdSpR, 47, 1529
Minnie, J., Bieber, J. W., Matthaeus, W. H., & Burger, R. A. 2007, ApJ, 670, 1149
Ngobeni, M. D., & Potgieter, M. S. 2012, AdSpR, 49, 1660
Nkosi, G. S., Potgieter, M. S., & Webber, W. R. 2011, AdSpR, 48, 1480
Parker, E. N. 1965, P&SS, 13, 9
Potgieter, M. S. 2000, JGR, 105, 18295
Potgieter, M. S. 2013, LRSP, 10, 1
Potgieter, M. S., & le Roux, J. A. 1989, A&A, 209, 406
Potgieter, M. S., Vos, E. E., Boezio, M., et al. 2014, SoPh, 289, 391
Richardson, J. D., Kasper, J. C., Wang, C., Belcher, J. W., & Lazarus, A. J. 2008, Natur, 454, 63
Richardson, J. D., & Wang, C. 2011, ApJL, 734, L1
Richardson, J. D., & Wang, C. 2012, ApJL, 759, L1
Scherer, K., & Fahr, H. J. 2003, AnGeo, 21, 1303
Scherer, K., & Ferreira, S. E. S. 2005a, ASTRA, 1, 17
Scherer, K., & Ferreira, S. E. S. 2005b, A&A, 442, L11
Shalchi, A., Bieber, J. W., & Matthaeus, W. H. 2004, ApJ, 604, 675
Snyman, J. L. 2007, Master's thesis, North–West Univ. (Potchefstroom Campus), South Africa (http://millennium.nwu.ac.za/record=b1703312∼S4)
Stone, E. C., Cummings, A. C., McDonald, F. B., et al. 2005, Sci, 309, 2017
Strauss, R. D., Potgieter, M. S., Ferreira, S. E. S., & Hill, M. E. 2010, A&A, 522, 1
Teufel, A., & Schlickeiser, R. 2002, A&A, 393, 703
Teufel, A., & Schlickeiser, R. 2003, A&A, 397, 15
Wang, C., & Belcher, J. W. 1999, JGR, 104, 549
Washimi, H., Zank, G. P., Hu, Q., et al. 2011, MNRAS, 416, 1475
Webber, W. R. 2005, JGR, 110, 1
Webber, W. R., & Intriligator, D. S. 2011, JGR, 116, 1
Whang, Y. C., Burlaga, L. F., & Ness, N. F. 1995, JGR, 100, 17015
Whang, Y. C., Burlaga, L. F., Wang, Y. M., & Sheeley, N. R. 2004, GeoRL, 31, 1
Zhao, L. L., Qin, G., Zhang, M., & Heber, B. 2014, JGR, 119, 1493